Available online at www.sciencedirect.com

ScienceDirect

Journal of Magnesium and Alloys 10 (2022) 400–410

www.elsevier.com/locate/jma

Full Length Article

Study of galvanic corrosion and mechanical joint properties of AZ31B and carbon-fiber–reinforced polymer joined by friction self-piercing riveting ☆

Yong Chae Lim*, Jiheon Jun*, Donovan N. Leonard, Yuan Li, Jian Chen, Michael P. Brady, Zhili Feng

Materials Science and Technology Division, Oak Ridge National Laboratory, One Bethel Valley Road, Oak Ridge, TN 37831, USA

Received 13 February 2021; received in revised form 10 April 2021; accepted 14 May 2021
Available online 17 June 2021

Abstract

A new testing methodology was developed to quantitively study galvanic corrosion of AZ31B and thermoset carbon-fiber–reinforced polymer spot-joined by a friction self-piercing riveting process. Pre-defined areas of AZ31B in the joint were exposed in 0.1 M NaCl solution over time. Massive galvanic corrosion of AZ31B was observed as exposure time increased. The measured volume loss was converted into corrosion current that was at least 48 times greater than the corrosion current of AZ31B without galvanic coupling. Ninety percent of the mechanical joint integrity was retained for corroded F-SPR joints to 200 h and then decreased because of the massive volume loss of AZ31B.

Keywords: Multi-material joining; Carbon fiber–reinforced polymer; AZ31B; Friction self-piercing riveting; Galvanic corrosion; Mechanical joint strength.

1. Introduction

Metal-to-composite hybrid structures represent a new concept for achieving higher specific strength (strength divided by density) for multi-material lightweight vehicles [1,2]. Their use enables greater fuel efficiency and lower greenhouse gas emissions. Higher–specific-strength alloys, such as magnesium (Mg) alloys and high-strength aluminum (Al) alloys, and advanced/ultra–high-strength steels are being considered as new materials for lighter vehicle structures. Also, carbon-fiber–reinforced polymer (CFRP) has been identified as a candidate engineering composite material with design flexibility and tailorable mechanical properties [3,4]. Among these materials, Mg alloys and CFRP have the highest potential for lightweight applications because of their higher specific strength [1].

However, the physical and chemical incompatibility of metals and polymer composites is a technical obstacle preventing the integration of such lightweight hybrid structures into unified body-in-white autobody assemblies that can meet joint performance and safety requirements. Extensive research and development efforts have been made to identify suitable processes for joining metal/composite material pairs to form assemblies. Joining techniques that have been tried include conventional fusion welding (laser welding, resistance spot welding) [5,6], solid-state joining [7-10], ultrasonic welding [11], mechanical fastening [12,13], and adhesive bonding [14]. Recently, a combination of the friction stir process

☆ This manuscript has been authored by UT-Battelle, LLC, under contract DE-AC05-00OR22725 with the US Department of Energy (DOE). The US government retains and the publisher, by accepting the article for publication, acknowledges that the US government retains a nonexclusive, paid-up, irrevocable, worldwide license to publish or reproduce the published form of this manuscript, or allow others to do so, for US government purposes. DOE will provide public access to these results of federally sponsored research in accordance with the DOE Public Access Plan (http://energy.gov/downloads/doe-public-access-plan).

* Corresponding author.
E-mail addresses: limy@ornl.gov (Y.C. Lim), junj@ornl.gov (J. Jun), leonarddn@ornl.gov (D.N. Leonard), liy5@ornl.gov (Y. Li), chenj@ornl.gov (J. Chen), bradymp@ornl.gov (M.P. Brady), fengz@ornl.gov (Z. Feng).

https://doi.org/10.1016/j.jma.2021.05.003

Table 1
Elemental compositions of AZ31B and steel rivet in weight percent for metallic elements and Si and in ppm for O and N. The compositions (wt.%) were analyzed by ICP-OES and combustion techniques.

	Mg	Fe	Al	Zn	Mn	Ni	Si	Cu	C	O	N
AZ31B	Balance	21 ppm	2.99	0.91	0.31	<10 ppm	<0.005	<10 ppm	–	–	–
Steel rivet	–	Balance	0.05	<0.01	0.74	0.01	0.04	0.01	0.18	<0.01	0.01

Table 2
Summary of mechanical and corrosion properties of thermoset CFRP, AZ31B, and steel rivet at room temperature (18).

Material	Ultimate tensile strength (MPa)	Elongation (%)	Corrosion potential
Thermoset CFRP	827	–	0.23 V_{SCE}
Steel rivet	463	26.4	−0.6 V_{SCE}
AZ31B	285	16.1	−1.55 V_{SCE}

(FSP) and self-piercing rivet (SPR) joining methods, called "friction self-piercing riveting" (F-SPR), has been proposed to join low-ductility materials such as Mg alloys and high-strength Al alloys [15-17]. This unique spot-joining process uses the friction heat from FSP and mechanical interlocking enabled by SPRs. Essentially, it involves a rivet that spins as it penetrates into stacked materials. The rotating rivet produces localized frictional heat as it interacts with the surrounding metal substrates. The generated friction heat increases the local ductility of the Mg alloy sheet to effectively avoid cracking problems. Most recently, the F-SPR process was further expanded to join a thermoset CFRP (TS-CFRP) to the Mg alloy AZ31B [18].

Another critical concern is galvanic corrosion in dissimilar material joints, particularly when Mg alloys are joined with noble metals. Accelerated Mg corrosion as a result of galvanic coupling can be indirectly assessed by comparing the corrosion potentials of individual joint components [19] or measuring the galvanic current between Mg and other components in simplified electrode configurations [20-23]. However, these indirect methods cannot fully emulate the galvanic corrosion of Mg in actual dissimilar material joints with more complex geometries. Another approach to evaluate Mg corrosion in dissimilar joints is to measure the corrosion mass loss [21,24]. Note that mass loss is the result of general and galvanic corrosion of Mg and other components in the joints, so Mg corrosion dominated by the galvanic effect may not be directly assessed. Therefore, a novel experimental design should be considered to permit the evaluation of Mg galvanic corrosion in specific dissimilar joints.

In the present work, a new methodology to study corrosion behavior was developed for the Mg alloy AZ31B joined to a TS-CFRP by F-SPR. In this method, a pre-defined AZ31B area in the F-SPR joint produced measurable corrosion loss during immersion in 0.1 M NaCl solution. Galvanic corrosion of AZ31B driven by a steel rivet head was quantitatively estimated by corrosion volume measurement and further analyzed by corrosion potential and galvanic current measurements. Optical microscopy was used to measure the corrosion volume of AZ31B in the corroded F-SPR joints. X-ray tomography and scanning electron microscope (SEM) equipped with energy-dispersive spectroscopy (EDS) were also employed to characterize the corroded F-SPR joints. Lap shear tensile testing was used to evaluate the mechanical strength of post-immersion (corroded) F-SPR joints, and fractographical characterization was also conducted to investigate the failure mode(s).

2. Materials and experimental methods

2.1. Materials

In this work, TS-CFRP (Clearwater Composites, Minnesota, USA) with a G-83 prepreg laminate reinforced with 50 wt.% of unidirectional carbon fibers (T700, Toray) was used as a top sheet. The stacking sequence of the carbon fiber layers was [0°/90°] with nine plies, resulting in a total thickness of 1.9 mm. An AZ31B sheet 2.36 mm thick (Buymetal.com) was employed as the bottom material. Japanese Industrial Standard G3507–2 carbon steel (SWCH18A) was used to fabricate the hexagonally shaped rivet head (9.525 mm width). The rivet stem diameter and leg length were 5.3 and 6 mm, respectively. A detailed drawing and dimensions of the steel rivet and pip die can be found in previous work [18]. Inductively coupled plasma–optical emission spectrometry (ICP-OES) and combustion techniques were employed to characterize the chemical makeup of individual materials for the present work; the results are summarized in Table 1. A summary of the mechanical and corrosion properties of each material are provided in Table 2 [18].

Water jet cutting was used to cut sheet materials into coupons with dimensions of 25.4 mm width and 101.6 mm length for lap shear coupons. Then, reagent acetone and alcohol were used to clean the surfaces of the AZ31B, and the TS-CFRP coupons were sonicated with an ethanol solution. Finally, all coupons were dried at room temperature before F-SPR joining.

2.2. Description of F-SPR process and joint fabrication

A description of the F-SPR process can be found in the authors' previous work [18], and a brief description of the join-

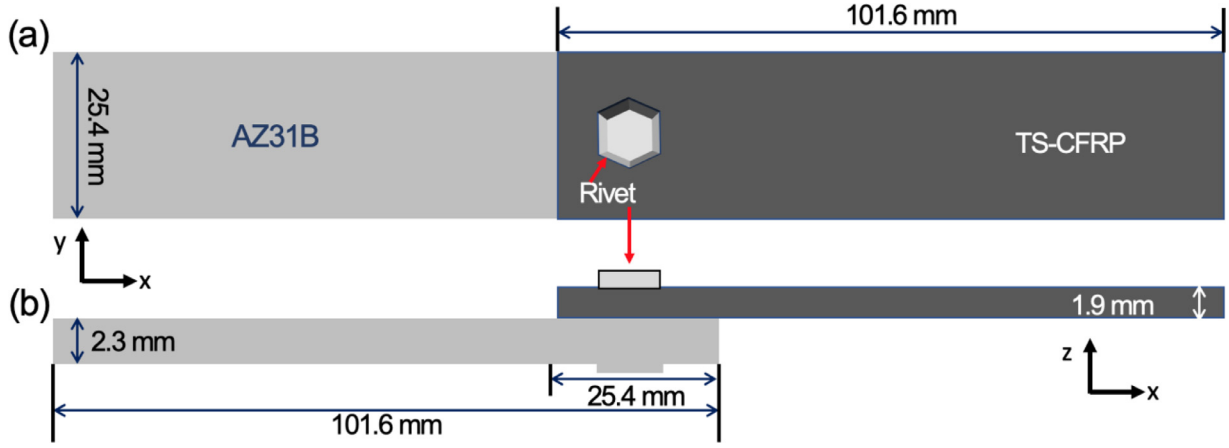

Fig. 1. A schematic of the lap shear joint configuration. The unit is mm.

Table 3
Summary of F-SPR parameters.

Spindle rotational speed (rpm)	1500
Downward plunge depth (mm)	6.12
Downward plunge speed (mm/s)	2.86

ing process is provided as follows. First, an external plunging axial force is used to drive a spinning rivet into a stacked workpiece. During this process, frictional heat is locally generated between the rivet and the bottom sheet metal (i.e., AZ31B), leading to improved local ductility of the AZ31B. Finally, the rivet leg flares out in the AZ31B based on the supporting die geometry, leading to mechanical interlocking in the workpiece. Fig. 1 illustrates a lap shear joint configuration with a 25.4 mm overlap size. Based on previous F-SPR trials, the joining process parameters summarized in Table 3 were selected with the highest lap shear failure load (˜5 kN) [18]. The lap shear joint specimens were used for the subsequent corrosion study.

2.3. Corrosion testing

2.3.1. Corrosion exposure of pre-defined AZ31B in F-SPR joint

To enable a quantitative assessment of Mg corrosion, a new testing method was applied to the F-SPR joints to expose the rivet head and pre-defined side sections of the AZ31B for the 0.1 M NaCl immersion test. A specific tape masking technique was applied to the F-SPR specimens and to the AZ31B side surfaces for corrosion exposure, as illustrated in Fig. 2a. The AZ31B area on one pre-defined side surface was 2.3×10 mm^2. An F-SPR lap joint during immersion testing is schematically depicted in Fig. 2b. After tape masking was applied, the active surfaces in contact with the solution were the two exposed sides of AZ31B (marked in Fig. 2b), the steel rivet, and the carbon fibers exposed on the sides of the CFRP. Also note that the solution was drawn into the narrow gap between the AZ31B and the CFRP by capillary force during immersion, allowing corrosion exposure of the joining section inside the gap. To measure the corrosion potential (E_{corr}) of an immersed F-SPR joint, a saturated calomel electrode (SCE) was placed adjacent to the overlap section of the joints. During immersion, the AZ31B side surfaces formed a corrosion volume as a result of anodic dissolution of the alloy by galvanic impact. The anodic dissolution of Mg from this pre-defined area is similar to the experimental concept used for one-dimensional artificial pits in stainless steels in which a quantifiable corrosion volume and depth were produced [25,26]. A similar method was also adopted to investigate galvanic corrosion of AZ31B and CFRP joined by steel bolting [27]. A side view of the corrosion volume formed on the AZ31B exposure surfaces is presented in Fig. 2c. After immersion testing, all F-SPR joints were cleaned ultrasonically in a deionized water bath and rinsed by reagent ethanol and water to remove corrosion products.

The corrosion volume of AZ31B was calculated by the sheet thickness (2.3 mm) and the corroded area estimated by an image analysis software. The calculated corrosion volume was then converted to the anodic charge using the charge balance, density, and molar mass of Mg, +2, −1.77 g·cm^{-3} and 24.3 g·mol^{-1}, respectively, and Faraday constant of 96,485 C•mol^{-1}. The anodic current was also determined from the anodic charge divided by the immersion time. Meantime, the electrode area of AZ31B during the immersion increased as the corrosion volume grew, so a nominal surface area (described in the appendix) was used to estimate the anodic current density.

In addition to the corrosion volume measurement, dummy lap specimens, which mimicked the actual F-SPR joints but with no connection between the AZ31B and the riveted CFRP, were used for galvanic current measurement. To prepare the dummy lap specimens, the F-SPR joints were cut to separate the AZ31B and riveted CFRP sheets, and then circular ($\varnothing = 12.7$ mm) and 25.4 mm wide insulating tapes were applied on the mating surfaces of the AZ31B and CFRP, respectively, as described in Fig. 3a and 3b. The separated AZ31B and CFRP were then re-assembled and tape-masked to expose the same AZ31B side surfaces and rivet head used in the immersion testing of the actual F-SPR joints depicted in

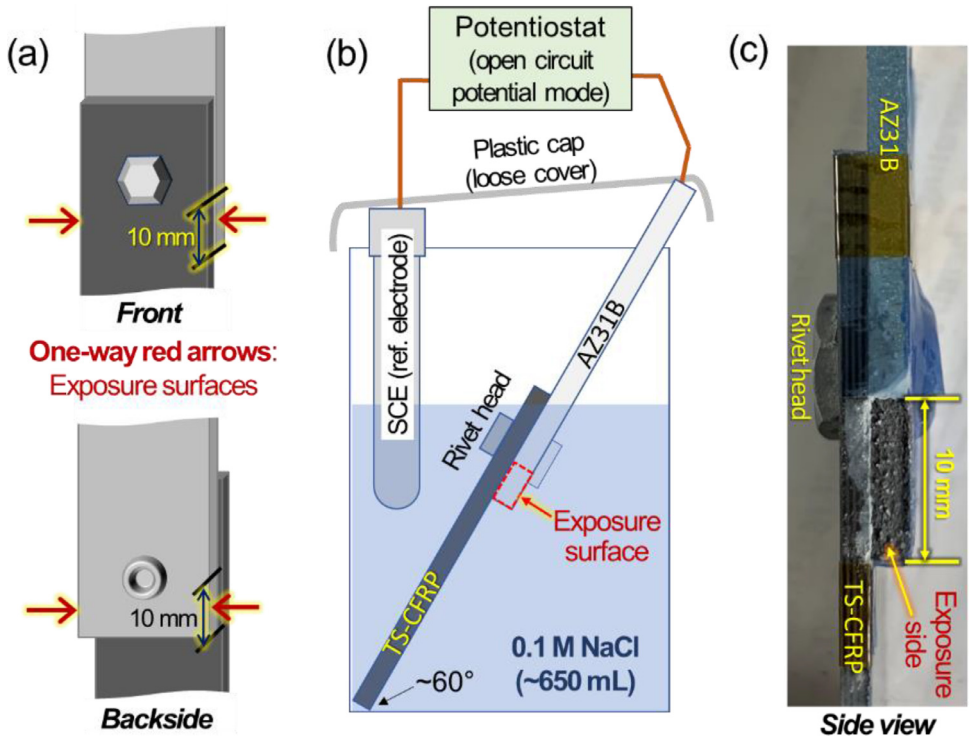

Fig. 2. Schematic descriptions of (a) the location of the AZ31B side surfaces for 0.1 M NaCl solution exposure and (b) the immersion testing with E_{corr} measurement. (c) A photo image of corroded AZ31B in an F-SPR joint after 25 h of immersion.

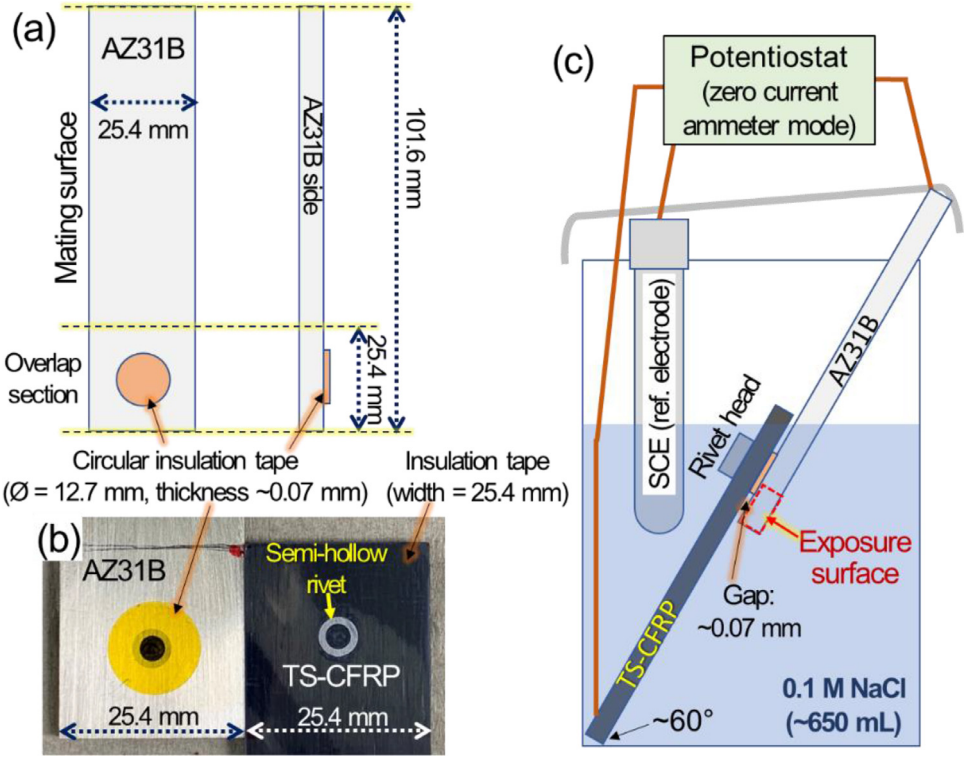

Fig. 3. Preparation and immersion testing of dummy lap specimens: (a) AZ31B mating surface with the location of the circular insulation tape, (b) a photo of AZ31B and CFRP mating surfaces after the application of insulation tapes, and (c) a schematic of galvanic current measurement from a dummy lap specimen.

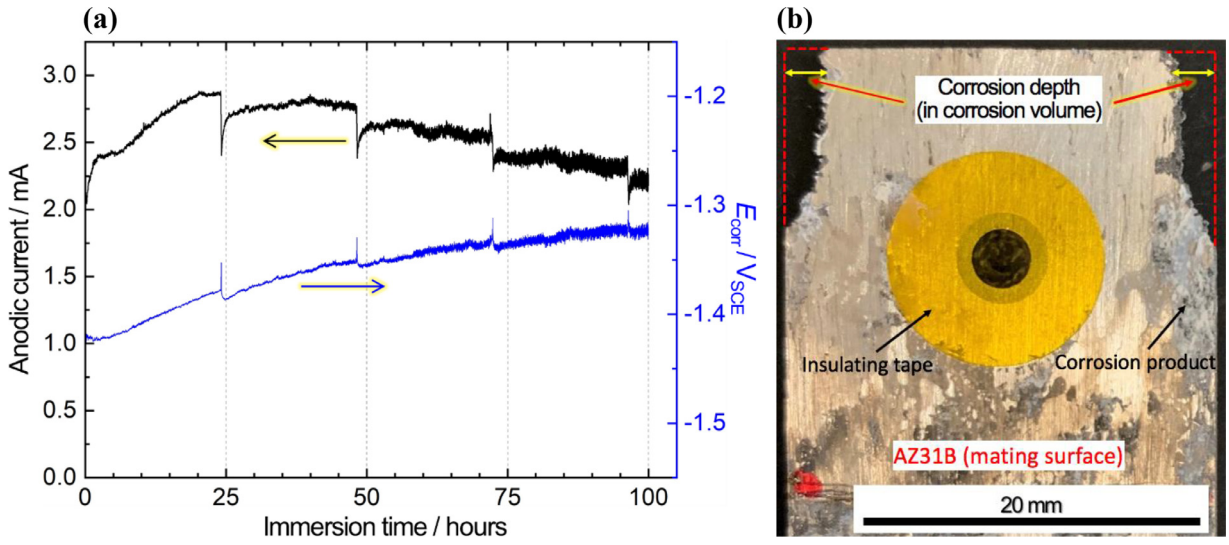

Fig. 4. Immersion testing of a dummy lap specimen: (a) measured anodic current and E_{corr} for 100 h and (b) a photo of the AZ31B mating surface after testing and cleaning. The mating surface clearly showed the corrosion volume and depth formed from the two exposed sides. . (For interpretation of the references to colour in this figure legend, the reader is referred to the web version of this article.)

Fig. 2a. The AZ31B and CFRP in the dummy lap specimens were connected individually to a potentiostat in zero current ammeter mode, and a reference SCE was placed near the overlap section to monitor the E_{corr} of the dummy lap specimen, as shown schematically in Fig. 3c. With the dummy lap samples, it was possible to measure the galvanic current between the rivet head and the AZ31B sheet in the same geometrical configuration as in the actual F-SPR joints. These dummy lap specimens also formed a corrosion volume, enabling the estimation of anodic current by using the same procedure stated previously in this section. All immersion testing was conducted at room temperature with loose plastic covers, as illustrated in Fig. 2b and Fig. 3c, to allow access of air but minimize the evaporation of the 0.1 M NaCl solution.

2.4. Metallographic preparation

The post-corrosion F-SPR samples were first mounted in epoxy and then cut into halves to obtain cross-sections using a diamond saw. The cross-sectioned samples were ground by silicon carbide papers with 600, 800, 1200 grits and then polished using diamond suspensions of 3 μm, 1 μm, and 0.5 μm.

2.5. Characterization of post-corroded samples

A digital optical microscope (Dino-Lite Edge, Taiwan) was used to characterize the post-corrosion F-SPR samples. DinoXcope software was used to measure the corrosion depth and volume for the corrosion-tested samples.

X-ray tomography was employed to study the post-corrosion F-SPR joints in three different viewing orientations as a nondestructive evaluation method. X-ray scans were acquired using a Zeiss Metrotom 800, operated at 180 kV with a 220 uA beam current. This tungsten source x-ray microscope achieved ~15 um resolution using a 1 mm thick copper filter. X-ray data were analyzed using a VGStudio Max 3.3 created by Visual Graphics GmbH.

SEM coupled with EDS (TESCAN Mira3) was used to characterize the cross-sectional view of the corroded F-SPR joint. An accelerating voltage of 20 kV was set during SEM. The elements Mg, Fe, O, and C were mapped with a scanning time of 4 min at the interfaces in the post-corroded samples.

2.6. Static lap shear tensile testing of F-SPR specimens

An MTS tensile machine was used to evaluate the joint strength of post-corrosion F-SPR coupons. Lap shear tensile testing was performed with a constant cross-head speed of 10 mm min^{-1} at room temperature. To minimize bending of the specimen during lap shear tensile testing, spacers (25.4 by 25.4 mm) were used to hold the lap shear coupons to align them vertically between the grips.

3. Results and discussion

3.1. Corrosion characterization

The anodic current and E_{corr} of a dummy lap specimen are presented in Fig. 4 along with a photo image showing the mating surface of the specimen after immersion testing. For 100 h of immersion testing, E_{corr} gradually increased with time and was higher than the reported E_{corr} of AZ31B alone, ~1.55 V_{SCE} in 0.1 M NaCl [28-31], indicating that the AZ31B in the dummy lap specimen was galvanically polarized. Meanwhile, the measured anodic current increased for an initial 25 h and then decreased gradually to ~2.2 mA afterward. The immersion testing of dummy lap specimens was conducted three times, once for 50 h and twice for 100 h. The average measured anodic currents and initial/final E_{corr} values are

Table 4
Summary of measured E_{corr} and average anodic currents as well as the corrosion-volume–calculated anodic currents from three dummy lap specimens.

Immersion time (h)	E_{corr} / V_{SCE}		Average measured anodic current / mA	Calculated anodic current by corrosion volume / mA	Note
	Initial	Final			
50	−1.44	−1.35	2.73	4.69	
100	−1.43	−1.32	2.57	5.31	Shown in Fig. 4
	−1.43	−1.34	2.41	4.84	
Avg. of three data sets			2.49±0.11	4.66±0.19	Average ± std. deviation

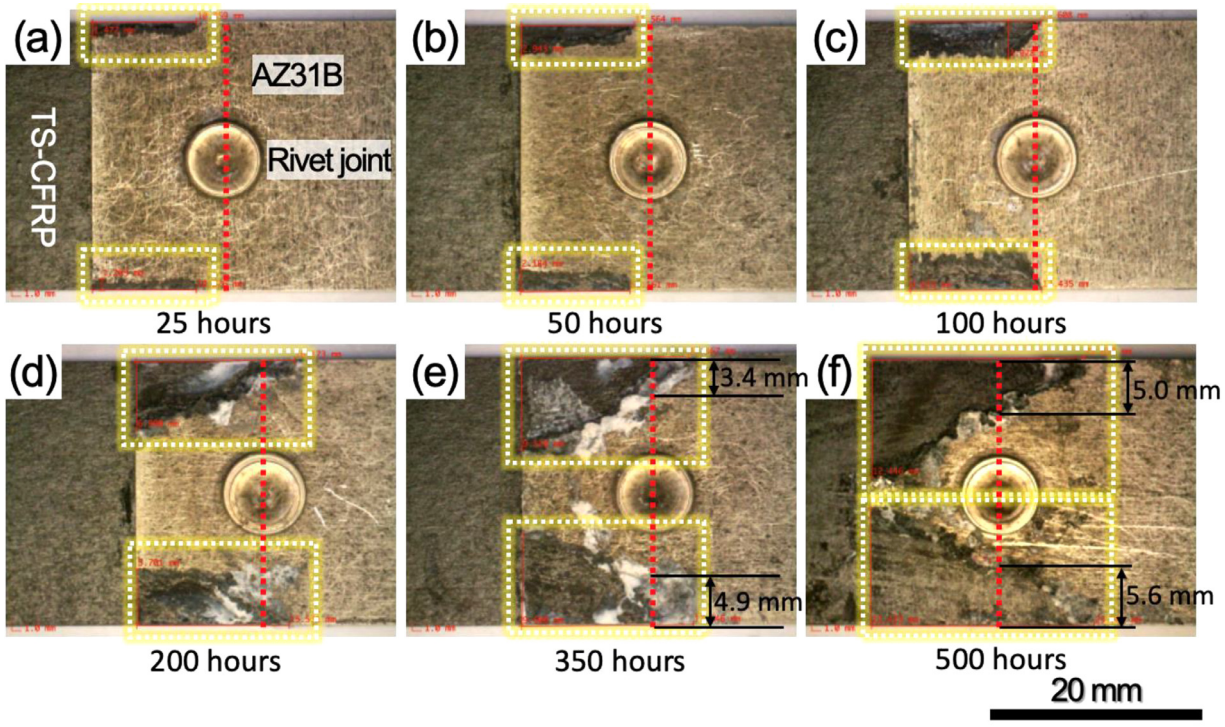

Fig. 5. Sequence of optical images for post-corrosion F-SPR joint (backside view) with different exposure times in 0.1 M NaCl solution; (a) 25 h, (b) 50 h, (c) 100 h, (d) 200 h, (e) 350 h, and (f) 500 h. Red dot line was added in the center of rivet joint to indicate how corrosion of AZ31B progressively reduces effective cross-sectional area at the rivet joint. (For interpretation of the references to colour in this figure legend, the reader is referred to the web version of this article.)

summarized along with the corrosion-volume-calculated anodic currents in Table 4. The measured anodic current is about 53% of the corrosion volume–based anodic current. This is the case because Mg anodic dissolution is balanced by a H_2 reduction reaction not only on the steel rivet but also on the Mg itself [32], indicating that the evolution of H_2 on the Mg surface accounted for the remaining 47% of anodic Mg dissolution. In the three measurements, the initial E_{corr} values were similar, but the final E_{corr} values were slightly higher for 100 h than 50 h.

Fig. 5 shows the examples of the corrosion volume formed on F-SPR joints for 25–500 h of immersion testing, during which galvanic corrosion of AZ31B (red dotted box) caused greater Mg loss with increasing exposure time. Overall, corrosion of AZ31B started from the pre-defined exposure location and propagated into the joint. Red dot line was added in the center of rivet joint to show the degree of corrosion progression in AZ31B. Up to 200 h of exposure time, the loss of AZ31B found did not extend to the center of rivet joint as indicated by red dot line in Fig. 5a-d. Therefore, effective cross-sectional area at the rivet joint was not as different from the non-corroded specimen. However, after 350 h testing, reduction of effective cross-sectional area at the rivet joint was observed in Fig. 5e-f. For example, 5˜5.6 mm of corrosion depth was found from edge of coupon to the center of rivet joint at 500 h. This loss of AZ31B at the joint effectively decreased the joint integrity as described in the following section.

The increasing corrosion volumes of AZ31B from the exposed F-SPR joints are plotted in Fig. 6a as a function of exposure time. In addition, the anodic current and current density, calculated from the corrosion volume data and plotted in Fig. 6b, decreased with immersion time. The calculated current density at 500 h was about 45% of the current density at 25 h, indicating that the dissolution rate of Mg at the corroding interface decreased as the corrosion volume and depth increased. The reduction in Mg dissolution was presumably caused by an increased solution ohmic drop as the corroded

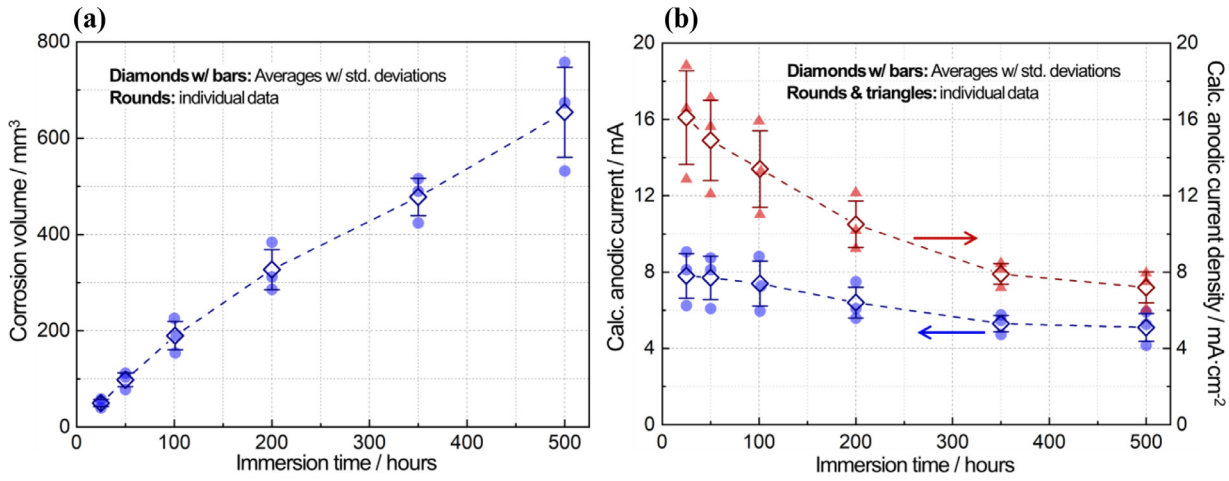

Fig. 6. F-SPR joint immersion testing results: (a) corrosion volume and (b) calculated anodic current and current density as a function of immersion time.

Table 5
Summary of measured E_{corr} from F-SPR joint immersion testing.

Immersion time (h)	E_{corr} / V_{SCE}		ΔE_{corr} (final-initial) / mV
	Initial	Final	
25	−1.45	−1.42	30
50	−1.44	−1.37	70
	−1.43	−1.35	80
100	−1.44	−1.31	130
200	−1.45	−1.28	170
350	−1.43	−1.26	170
500	–	−1.23	–
	–	−1.26	–
	–	−1.27	–

volume of AZ31B was occupied by solid phase corrosion products. The measured E_{corr} during the immersion testing of the F-SPR joints is summarized in Table 5. The initial E_{corr} ranged from −1.43 to −1.45 V_{SCE}, similar to the values measured from the dummy lap specimens (see Table 4). E_{corr} increased with time to 200 h but there was no further increase afterward, as seen from the ΔE_{corr} values. The values of final E_{corr} were similar between 350 and 500 h. The increase in E_{corr} is again considered to occur as a result of the increased ohmic drop from the buildup of solid corrosion products.

For 50 and 100 h immersion testing, the anodic currents for the F-SPR joints in Fig. 6b were higher than the current calculated from the corrosion volume of the dummy specimens (Table 4), but their E_{corr} values were not notably different from each other (Table 4 and Table 5). With the similar E_{corr} of AZ31B in the F-SPR joints and dummy specimens, it is reasonable to assume the following:

$$\eta_1 + I_1R_1 \approx \eta_2 + I_2R_2 \quad (1)$$

where η is the overpotential applied to AZ31B, I is galvanic current between AZ31B and the steel rivet, R is the total resistance for the galvanic current flow, and the subscripts 1 and 2 indicate that the values are for F-SPR joints and dummy samples, respectively. With higher anodic currents for AZ31B in the F-SPR joint, η_1 and I_1 should be greater than η_2 and I_2, meaning that R_2 must have been greater than R_1 to satisfy Eq. (1). Both R_1 and R_2 must have very similar solution resistance components, implying that the solid path resistance component was greater in the dummy samples. This inference is reasonable, as the solid conduction path in the dummy samples was through carbon fibers and electric wires without direct contact between the AZ31B and the steel rivet (as was the case in the F-SPR joints).

The corrosion current density data from this work and from the literature are compared for AZ31B and unalloyed Mg in Fig. 7. The lowest value of the corrosion current density, ~7.2 mA·cm^{-2}, in this work was about 48 times greater than the highest current density value from the literature, ~0.15 mA·cm^{-2}, giving a quantitative measure of the lower-limit galvanic influence for AZ31B in the F-SPR joint configuration. More generally, it can be said that AZ31B galvanically coupled with a bare steel rivet in F-SPR lap joints corrodes 2–3 orders more than in the same alloy without galvanic polarization [31,33,34]. Meanwhile, the corrosion current densities of unalloyed Mg were slightly lower than those of AZ31B in the compared literature data [35-37].

3.2. Characterizations of corroded F-SPR joints

Fig. 8 shows X-ray tomographic images for an F-SPR joint after 500 h of corrosion, at three different viewing orientations. Fig. 8a depicts massive galvanic corrosion of Mg (yellow dotted lines), which is correlated with a joint that underwent corrosion for 500 h (Fig. 5f). A cross-sectional view of the corroded F-SPR joint is shown in Fig. 8b and 8c in different viewing planes (z-y and x-z planes). In Fig. 8b, it is seen that both edges of the AZ31B (yellow dotted boxes) significantly corroded as the area was directly exposed to 0.1 M NaCl. However, there is no obvious corrosion of the steel rivet and the AZ31B at the left side (red dotted circle, labeled "1″) and the right side of the joint (orange dot circle, labeled "2″). This result could be due to the limited corrosion solution infiltration into the joint area because of the tight gap tolerance between the TS-CFRP and AZ31B. Also, mechanical inter-

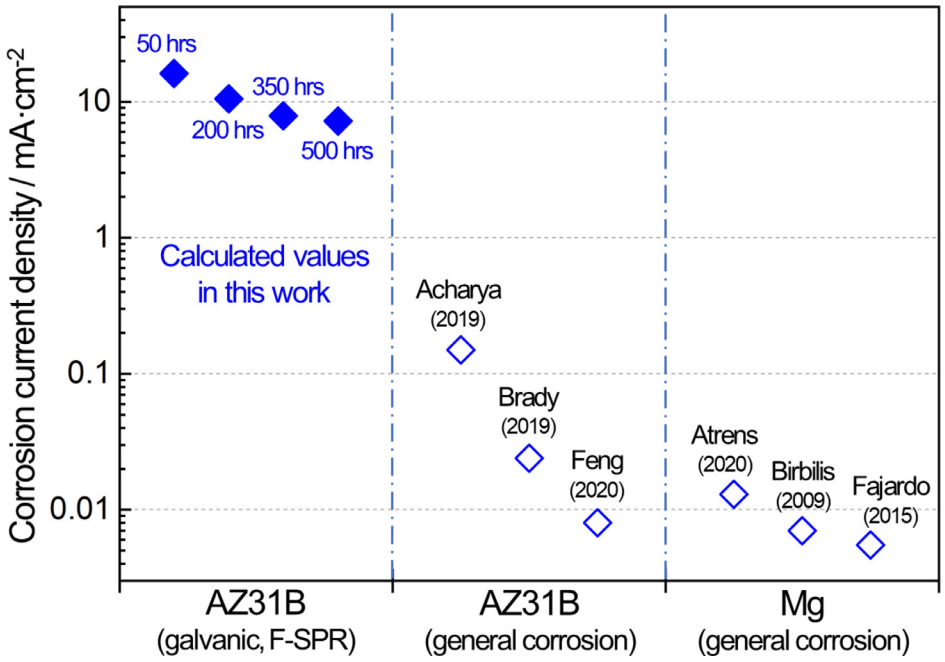

Fig. 7. Comparison of corrosion current for AZ31B under galvanic influence in F-SPR joints (this work) and with no galvanic influence (31, 33, 34). The corrosion current of unalloyed Mg without galvanic impact (35–37) is also included. Five literature corrosion currents were measured in 0.1 M NaCl open to air at room temperature, but one data (37), converted from 0.3 mm•y^{-1} for high purity Mg in concentrated NaCl solutions, was deduced from multiple literature. . (For interpretation of the references to colour in this figure legend, the reader is referred to the web version of this article.)

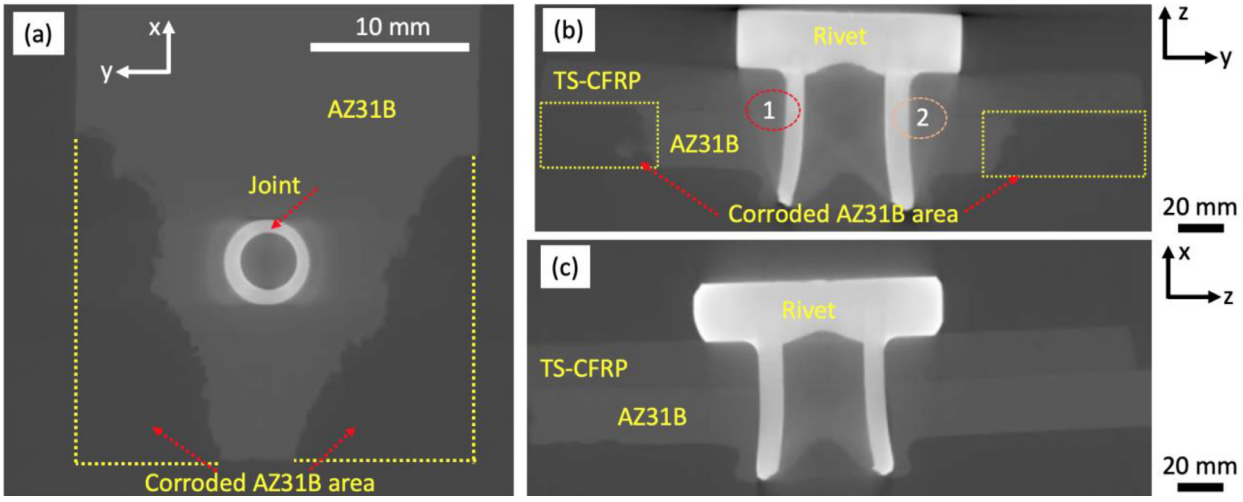

Fig. 8. X-ray tomographic images for 500 h corroded F-SPR joint at different viewing orientations: (a) x-y plane, (b) y-z plane, (c) x-z plane.

locking between the flared rivet leg and the bottom AZ31B sheet is observed in Fig. 8b and 8c. The interlocking distance was approximated 0.5 mm from our recent work [18]. This interlocking distance is the most important joint strength factor because it governs the locking strength between the rivet and the bottom sheet. Detailed characterization was conducted using SEM with EDS at the left side of the joint (red dotted circle) and is discussed in the following section.

A cross-section of the F-SPR joint after 500 h of corrosion was characterized by SEM with element maps at the left side of the joint interface (TS-CFRP – steel rivet – AZ31B), as previously shown in Fig. 8b (red dotted circle). In Fig. 9a, the SEM image clearly shows the joint interface with three materials: TS-CFRP, steel rivet, and AZ31B. First, part of the AZ31B was embedded into the TS-CFRP layer when the steel rivet plunged into the AZ31B. Second, there was no obvious corrosion of the steel rivet, potentially because of the limited electrolyte access into the joint. This finding agrees with the observation from x-ray tomography in Fig. 8b and 8c. Next, carbon fibers dripped into the joint interface between the steel rivet and the AZ31B because of the joining process (i.e., rotating and plunging motion of the rivet), producing a quite complex joint interface with intermixed materials. Finally, no significant corrosion of AZ31B was observed at the joint interface. There is physical contact between the steel rivet and the AZ31B; however, the limited access of the corrosion so-

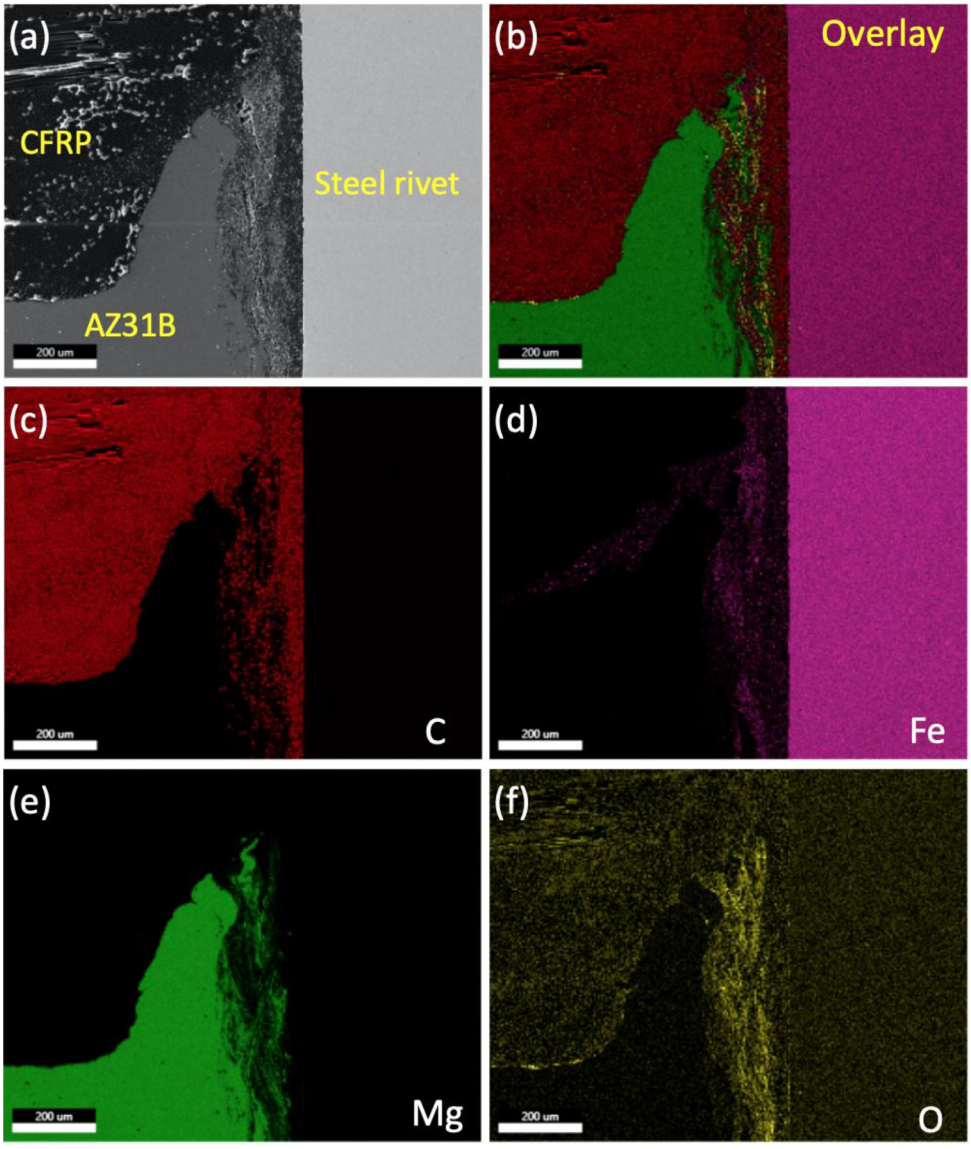

Fig. 9. SEM images with element maps for 500 h corroded F-SPR joints. (a) SEM image at the joint interface as shown in Fig. 8b, (b) overlay image of single elements (C, Fe, Mg, and O), (c) element map for C, (d) element map for Fe, (e) element map for Mg, and (f) element map for O.

lution into the joint, due to the tight gap between the AZ31B and TS-CFRP, practically limited the formation of a galvanic circuit at the joint interface. Note that another type of mechanical fastener, an SPR similar to that used in the current joining process, has the capability to achieve watertight joints by tightly clamping the materials during the joining process [38]. On the other hand, the exposure areas on both sides of the AZ31B, as preciously shown in Fig. 5 and Fig. 8a, were significantly corroded as a result of galvanic coupling and direct exposure to the 0.1 M NaCl solution.

3.3. Mechanical joint strength for post-corroded F-SPR joints and fractography

The mechanical joint integrity of the F-SPR joint under different corrosion exposure times was evaluated by lap shear tensile testing. Fig. 10 summarizes the averaged peak failure load at different testing times. The average lap shear failure load for an uncorroded F-SPR joint was around 5 kN

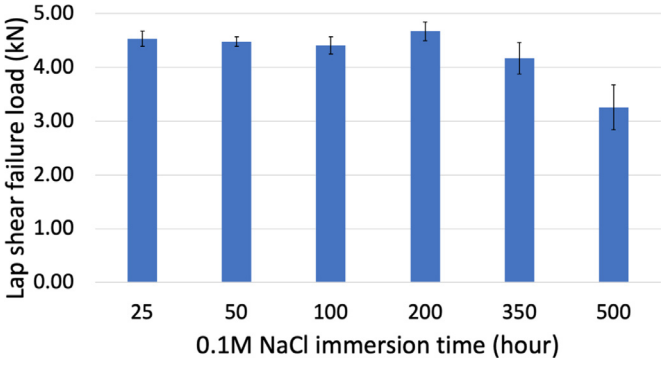

Fig. 10. Summary of mechanical joint strength for post-corroded F-SPR joints at different exposure times.

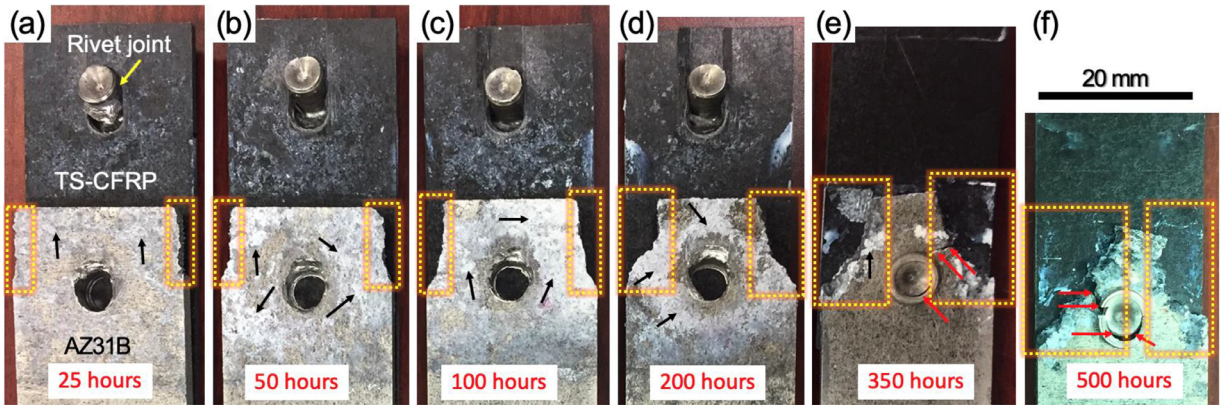

Fig. 11. Fractography of post-corroded F-SPR joints at different corrosion testing times after lap shear tensile testing. (a) 25 h, (b) 50 h, (c) 100 h, (d) 200 h, (e) 350 h, and (f) 500 h. Yellow dotted boxes at both edges of the AZ31B are corroded areas. The rivet joint is indicated by a yellow arrow. White corrosion product (black arrow) is seen at the joint. Cracking (red arrow) on AZ31B was seen for 350 h and 500 h exposure times. . (For interpretation of the references to colour in this figure legend, the reader is referred to the web version of this article.)

[18]. In general, nearly 90% of the averaged peak fracture load was retained during testing for up 200 h. Then, the joint strength started to decrease from 350 h of exposure time, and 83.4% of the strength of the untested F-SPR joint remained. Finally, 65% of the original F-SPR joint strength was retained at 500 h. This decrease of joint strength can be related to the reduction of effective cross-sectional area at the rivet joint as illustrated in Fig. 5. However, Fig. 9 shows no significant corrosion at the joint interface. Therefore, the fracture surfaces of the F-SPR joint were evaluated.

A summary of fractography images at the mating joints is provided in Fig. 11. As the corrosion exposure time increases, both edges of the AZ31B show greater corrosion loss. However, as shown in Fig. 11a–d, the failure mode of the F-SPR joints for up to 200 h was not changed from that of the uncorroded F-SPR joints (i.e., AZ31B pullout, indicated by the yellow arrow in Fig. 11a, due to the strong mechanical interlocking between the flared rivet leg and the AZ31B. This is because the loss of AZ31B did not impact the effective cross-sectional area at the rivet joint (red dot line in Fig. 5) up to 200 h as discussed previously. A white corrosion product (black arrow) on the AZ31B and TS-CFRP surfaces was seen at the edges, but no significant amount of corrosion product was found at the joint. The white corrosion products must be the mixture of Mg oxide and hydroxides that were commonly found on corroded AZ31B [39-41]. Again, the tight gap between the TS-CFRP and AZ31B was considered to have limited the infiltration of the corrosion solution into the joint. Thus, no significant joint strength reduction was found until after 200 h of exposure time. However, cracking (red arrow) was observed away from the joint after 350 and 500 h exposure time, as seen in Fig. 11e and 11f. This cracking is related to massive galvanic corrosion of AZ31B at the joint, resulting in a great reduction in the effective cross-sectional area at the joint. Also, localized corrosion of AZ31B may have created several crack initiation sites during the lap shear tensile testing and resulted in crack propagation into the joint area. Thus, after 350 h of immersion in the solution, the F-SPR joint strength started to degrade because the effective joint volume of the AZ31B was greatly reduced.

The present works provides a unique methodology to quantitively study the galvanic corrosion of Mg alloy with the other materials (e.g., steel rivet and CFRP) in the actual dissimilar material joints. This protocol can be used to investigate the impacts of coating and other mitigations efforts to improve the galvanic corrosion resistance, directed to the AZ31B, the CFRP, and the steel rivet.

4. Conclusion

In the present work, a new method was introduced for quantitative investigation of galvanic corrosion attack on AZ31B by other materials (i.e., steel rivets and TS-CFRP) in F-SPR joints. The corrosion current densities of AZ31B under galvanic impact was determined by measuring the corrosion volume, which was at least 48 times greater than the corrosion current density with no galvanic coupling. X-ray tomography and SEM characterizations for post-corroded F-SPR joints revealed that the inter-joint area was not significantly corroded because the solution had limited access into the tight gap between the TS-CFRP and AZ31B in the joint. Mechanical joint integration was retained at almost 90% of that of the original F-SPR joint for testing up to 200 h. However, the strength of the F-SPR joint started to decrease after 350 h of exposure because of the large volume loss of AZ31B in the joint. The failure mode of corroded F-SPR joints was pullout of AZ31B until after 200 h of exposure, which was the same failure mode as for uncorroded F-SPR joints. Subsequently, the failure mode of corroded F-SPR joints changed to base AZ31B failure as a result of massive loss of AZ31B volume in the joint.

Author contribution

Conceptualization, Y.C. Lim, J. Jun; Methodology, Y.C. Lim, J. Jun; Investigation, Y.C. Lim, J. Jun, D. Leonard, Y.

Li, J. Chen; Data curation, Y.C. Lim, J. Jun, M.P. Brady; Roles/writing—original draft, Y.C. Lim, J. Jun, D. Leonard, Y. Li; Writing—review and editing, Y.C.L, J. Jun, M.P. Brady, Z. Feng; Supervision, M.P. Brady, Z. Feng.

Acknowledgments

This research was financially sponsored by the US Department Energy Vehicle Technologies Office, as part of the Joining Core Program. Oak Ridge National Laboratory (ORNL) is managed by UT-Battelle LLC for the US Department of Energy under Contract DE-AC05-00OR22725. The authors would like to thank Donald Erdman III and Rick R. Lowden for their help in the mechanical testing laboratory.

Appendix

The nominal surface area of AZ31B during corrosion was estimated using the corrosion depths described in Fig. A1. The surface area at the end of the corrosion exposure was estimated as 2.3 mm × (d_1 + 10 mm) for one side and 2.3 mm × (d_2 + 10 mm) for the other side, making the total area 2.3 mm × (d_1 + d_2 + 20 mm). The initial and final areas, 46 mm^2 and 2.3 mm × (d_1 + d_2 + 20 mm), respectively, were averaged to define the nominal surface area as 1.15 mm × (d_1 + d_2 + 40 mm). Note that the AZ31B area in the mating surface was not considered for the nominal surface area because the rate of Mg dissolution on the mating surface was considered to be much lower than the dissolution rate on the side surfaces.

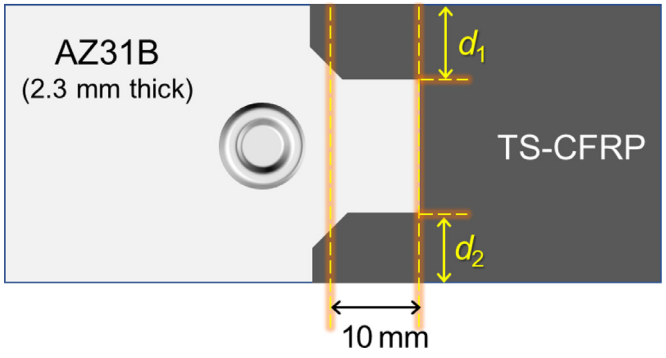

Fig. A1. A schematic description of corroded Mg in an F-SPR joint with the measured depths, d_1 and d_2, used to calculate the nominal surface area for anodic current density calculation. .

References

[1] S. Kleinbaum, C. Jiang, S. Logan, MRS Bull. 44 (2019) 608–612.
[2] U. Dilthey, L. Stein, Sci. Technol. Weld. Join. 11 (2006) 135–142.
[3] H. Adam, Mater. Des. 18 (1997) 349–355.
[4] K.L. Edwards, Mater. Des. 19 (1998) 1–10.
[5] Z. Zhang, J. Shan, X. Tan, J. Zhang, Int. J. Adv. Manuf. Technol. 90 (2017) 3465–3472.
[6] K. Nagatsuka, et al., Sci. Technol. Weld. Join. 23 (2018) 181–186.
[7] S.M. Goushegir, J.F. dos Santos, S.T. Amancio–Filho, Mater. Des. (1980-2015) 54 (2014) 196–206.
[8] J.V. Esteves, et al., Mater. Des. 66 (2015) 437–445.
[9] Y.C. Lim, et al., Metals (Basel) 8 (2018) 865.
[10] K. Nagatsuka, S. Yoshida, A. Tsuchiya, K. Nakata, Compos. Part B: Eng. 73 (2015) 82–88.
[11] F. Balle, G. Wagner, D. Eifler, Adv. Eng. Mater. 11 (2009) 35–39.
[12] J. Min, Y. Li, J. Li, B.E. Carlson, J. Lin, Int. J.f Adv. Manuf. Technol. 76 (2015) 1403–1410.
[13] S. Wang, J. Min, J. Lin, H. Wan, Y. Wang, Weld. World 63 (2019) 1013–1024.
[14] X. Liu, X. Shao, Q. Li, G. Sun, Compos. Part B: Eng. 172 (2019) 339–351.
[15] Y. Li, Z. Wei, Z. Wang, Y. Li, J. Manuf. Sci. Eng. 135 (2013).
[16] X. Liu, et al., J. Mater. Process. Technol. 237 (2016) 19–30.
[17] Y. Ma, M. Lou, Y. Li, Z. Lin, Weld. World 62 (2018) 1195–1206.
[18] Y.C. Lim, et al., J. Manuf. Sci. Eng.-Trans. Asme 143 (2021) 031006–031001.
[19] M. Mandel, L. Krüger, Corros. Sci. 73 (2013) 172–180.
[20] Y.C. Lim, et al., Mater. Des. 69 (2015) 37–43.
[21] D.R. Banjade, S.D. Porter, B.M. McMullan, J.N. Harb, J. Electrochem. Soc. 163 (2016) C116–C123.
[22] R.C. McCune, J.H. Forsmark, V. Upadhyay, D. Battocchi, in Magnesium technology 2015, M. V. Manuel, A. Singh, M. Alderman, N. R. Neelameggham, Eds. (Springer International Publishing, Cham, 2016), pp. 327–332.
[23] V. Upadhyay, et al., SAE Int. J. Mater. Manf. 9 (2016) 187–199.
[24] Y. Zheng, et al., Materials (Basel) 12 (2019).
[25] J. Jun, G.S. Frankel, N. Sridhar, J. Solid State Electrochem. 19 (2015) 3439–3447.
[26] J. Jun, T. Li, G.S. Frankel, N. Sridhar, Corros. Sci. 173 (2020) 108754.
[27] J. Jun, Y.C. Lim, Y. Li, C.D. Warren, Z. Feng, Materials (Basel) 14 (2021).
[28] T. Cain, L.G. Bland, N. Birbilis, J.R. Scully, Corrosion 70 (2014) 1043–1051.
[29] Z. Feng, B. Hurley, J. Li, R. Buchheit, J. Electrochem. Soc. 165 (2018) C94–C102.
[30] G. Williams, H. Ap Llwyd Dafydd, R. Subramanian, H.N. McMurray, Corrosion 73 (2017) 471–481.
[31] M.G. Acharya, A.N. Shetty, J. Magnesium Alloys 7 (2019) 98–112.
[32] T. Cain, S.B. Madden, N. Birbilis, J.R. Scully, J. Electrochem. Soc. 162 (2015) C228–C237.
[33] M.P. Brady, et al., J. Electrochem. Soc. 166 (2019) C492–C508.
[34] Z. Feng, J. Li, Z. Yang, R. Buchheit, Materials (Basel) 13 (2020) 1325.
[35] S. Fajardo, G.S. Frankel, Electrochim. Acta 165 (2015) 255–267.
[36] N. Birbilis, M.A. Easton, A.D. Sudholz, S.M. Zhu, M.A. Gibson, Corros. Sci. 51 (2009) 683–689.
[37] A. Atrens, et al., J. Magnesium Alloys 8 (2020) 989–998.
[38] D. Li, A. Chrysanthou, I. Patel, G. Williams, Int. J. Adv. Manuf. Technol. 92 (2017) 1777–1824.
[39] M.P. Brady, et al., J Electrochem Soc 167 (2020) 131513.
[40] M.F. Montemor, A.M. Simões, M.J. Carmezim, Appl. Surf. Sci. 253 (2007) 6922–6931.
[41] L. Wang, T. Shinohara, B.-P. Zhang, J. Solid State Electrochem. 14 (2010) 1897–1907.